ROYAL SOCIETY
OF CHEMISTRY

PAPER

Check for updates

Failure mechanism of solid-state electrolyte Li$_{10}$GeP$_2$S$_{12}$ in a moist atmosphere: a first-principles study

Jin Zhang,[a] Li Huang [ID][bc] and Xiao Gu [ID]*[a]

All-solid-state lithium-ion batteries (ASSLIBs) have commercial potential for industrial applications in long-range electric vehicles. The chemical properties of solid-sate electrolytes (SSEs) play a key role in the performance of ASSLIBs. Among all kinds of SSEs, sulfide solid-sate electrolytes are advantageous to ASSLIBs due to their high ionic conductivity and excellent electrochemical stability. However, sulfide electrolytes have poor stability in air due to their propensity to react with H_2O to generate toxic H_2S gas. Herein to understand the specific failure mechanism, we use first-principles calculations to study the kinetic and thermodynamic mechanism of the reaction between Li$_{10}$GeP$_2$S$_{12}$, which is a typical sulfide electrolyte, and H_2O in the atmosphere. We find that the H_2O molecules preferentially react with the sulfur atoms of the PS$_4$ tetrahedra to produce H_2S. As the sulfur atoms of the PS$_4$ tetrahedra in the bulk continuously emerge towards the surface, this reaction occurs repeatedly. Meanwhile, the oxygen atoms from H_2O molecules can also diffuse into the bulk. These reactions continue until the sulfur atoms of the PS$_4$ tetrahedra in Li$_{10}$GeP$_2$S$_{12}$ are completely replaced by oxygen atoms. Furthermore, we study the influence of Sb doping on Li$_{10}$GeP$_2$S$_{12}$, and kinetically explain the mechanism of hydrolysis inhibition when doping Sb in Li$_{10}$GeP$_2$S$_{12}$.

Introduction

With the growing demand for low-carbon technologies, lithium-ion batteries with a higher energy density, longer cycle life and better safety have become much more desirable to compete with gasoline vehicles. Traditional commercial lithium-ion batteries with a liquid organic electrolyte have the advantages of high theoretical specific capacity, environmental friendliness, *etc.*[1–5] However, the organic electrolyte in lithium-ion batteries is flammable, and has a lower thermal stability and lower safety compared with inorganic solid-state electrolytes.[6–8] The solid-state electrolytes used in solid-state lithium-ion batteries consist mainly of polymers,[9,10] oxides[11–13] and sulfides.[14,15] Among them, sulfides have a relatively high ionic conductivity, and some are comparable to organic liquid electrolytes.[16] However, sulfide solid-state electrolytes react easily with H_2O in moist air to generate toxic H_2S gas, which limits their practical applications. A great deal of experimental

work has been done to solve the air-stability problem. Muramatsu *et al.*,[17] have studied the structural changes of Li$_2$S–P$_2$S$_5$ glass structures in the atmosphere. This study found that PS$_4$$^{3-}$ can reduce H_2S gas for binary Li$_2$S–P$_2$S$_5$ glass or glass ceramics. 75Li$_2$S–25P$_2$S$_5$ has been found to have better water stability. Tin sulfides (Li$_4$SnS$_4$,[18,19] and Li$_4$SnS$_4$-LiI[20]), As-substituted Li$_4$SnS$_4$,[21] and Sb-substituted Li$_4$SnS$_4$[22,23] also show better stability in air. Based on the hard and soft acids and bases (HSAB) theory,[24] P is a hard acid, Sn, Sb, and As are soft acids, and S is a soft base, Thus, the Sn–, Sb–, and As–S bonds are harder than the P–S bond. Hayashi *et al.*[25] inhibited the production of H_2S by doping M$_x$O$_y$ (M = Fe, Zn, and Bi) in the Li$_3$PS$_4$ electrolyte, which can absorb H_2S. Although metal oxide doping improves the air stability of sulfide solid-state electrolytes, it also reduces the ionic conductivity. In addition, Sun *et al.*[26] improved the air stability of the sulfide solid-state electrolyte through introducing soft acid metals. The air stability is improved *via* Sb doping of Li$_{10}$GeP$_2$S$_{12}$, where the Li$_{10}$Ge(P$_{1-x}$Sb$_x$)$_2$S$_{12}$ ionic conductivity is 17.3 $\pm$ 0.9 mS cm^{-1}. After air exposure, the ionic conductivity can remain between 12.1 and 15.7 mS cm^{-1}.

Kamaya *et al.* reported a superionic conductor Li$_{10}$GeP$_2$S$_{12}$ with high ionic conductivity (12 mS cm^{-1}) at room temperature.[27] Compared with most sulfide solid-state electrolytes, Li$_{10}$GeP$_2$S$_{12}$ has been more extensively studied. Its space

[a] *School of Physical Science and Technology, Ningbo University, Ningbo 315211, China. E-mail: guxiao@nbu.edu.cn*

[b] *Guangdong Provincial Key Laboratory of Energy Materials for Electric Power, Academy for Advanced Interdisciplinary Studies, Southern University of Science and Technology, Shenzhen 518055, China*

[c] *Department of Physics, Southern University of Science and Technology, Shenzhen, Guangdong 518055, China*

group is $P42/nmc$, and consists of $(Ge_{0.5}P_{0.5})S_4$ tetrahedra, PS_4 tetrahedra, LiS_4 tetrahedra and LiS_6 octahedra. It has three-dimensional lithium-ion channels.[27–29] The diffusion paths along the c direction are considered as the dominant transport channel with the activation barrier of 0.16 eV, which is much lower than the diffusion barrier in the ab plane (0.26 eV).[30] In addition, $Li_{10}GeP_2S_{12}$ also has a wide electrochemical stability window (> 5 V against Li/Li$^+$) at room temperature. Mo et al.[29] proposed that this is due to the decomposition of $Li_{10}GeP_2S_{12}$ into Li_2S and P_2S_5 passivation layers when $Li_{10}GeP_2S_{12}$ comes into contact with the electrode, which then protects the solid-state electrolyte, resulting in a wide electrochemical window. However, as with other sulfide compounds, $Li_{10}GeP_2S_{12}$ is sensitive to atmospheric moisture, which can react with H_2O to produce the air pollutant H_2S,[31,32] and lead to a decreased ionic conductivity for $Li_{10}GeP_2S_{12}$. These drawbacks limit the practical applications of sulfide solid electrolytes in industry. Although a lot of research into $Li_{10}GeP_2S_{12}$ air stability has been carried out experimentally, few theoretical studies have been performed to explore the $Li_{10}GeP_2S_{12}$ air stability. In this work, we systematically study the specific chemical reactions between $Li_{10}GeP_2S_{12}$ and H_2O in air based on first-principles calculations, and explore the failure mechanism of the solid-state electrolyte in a moist atmosphere.

Computational details

All calculations are performed based on density functional theory (DFT) using the generalized gradient approximation (GGA) with the Perdew–Burke–Ernzerhof (PBE) functional.[33] The interactions between ion cores and valence electrons are treated using the projector augmented wave (PAW)[34,35] method as implemented in the Vienna ab initio simulation package (VASP).[36] The kinetic energy cutoff is set as 450 eV. In addition, the climbing image nudged elastic band (CI-NEB) method[37] is used to obtain the specific chemical reaction paths. A $4 \times 4 \times 1$ Monkhorst–Pack k-point grid is used to calculate the reaction coordinates and surface energies. All structures are fully relaxed until the residual forces are less than 0.01 eV Å^{-1} with the spin-polarized calculations. The crystal structure of $Li_{10}GeP_2S_{12}$ is shown in Fig. 1. The calculated lattice constants are $a = b = 8.74$ Å, and $c = 12.86$ Å, which are consistent with an earlier report.[38]

Results and discussion

In order to find the dominant surface of $Li_{10}GeP_2S_{12}$, we first obtain the surface energies (E_S) of various surfaces, which are calculated using eqn (1),

$$E_s = \frac{1}{2S}(E_{slab} - nE_{bulk}) \qquad (1)$$

where S is the surface area, E_{slab} is the total energy of the surface structure, n is the number of unit cells, and E_{bulk} is the total energy of bulk $Li_{10}GeP_2S_{12}$. As listed in Table 1, we find that the most stable surface is the (110) surface, which has
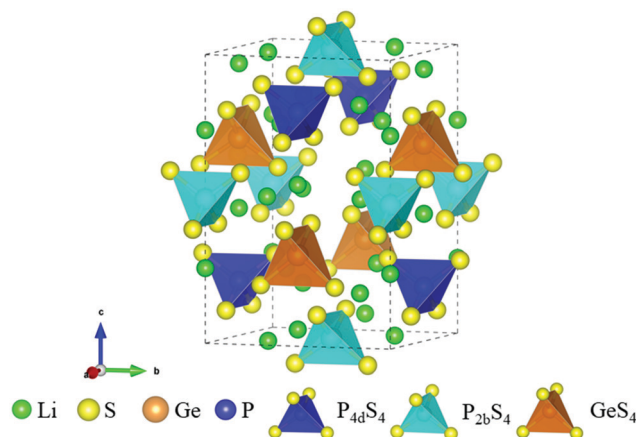

Fig. 1 Crystal structure of $Li_{10}GeP_2S_{12}$.

Table 1 Surface energy (E_S) values of $Li_{10}GeP_2S_{12}$

Surface	E_S (eV Å^{-2})
(001)	0.033
(010)	0.075
(100)	0.059
(110)	0.029
(011)	0.055
(101)	0.064
(111)	0.040

lowest energy of 0.029 eV Å^{-2}. According to the results of the surface energies, the (001) and (110) surfaces are more likely to be exposed to the air. However, we find that there are both PS_4 tetrahedra and GeS_4 tetrahedra on the exposed (110) surface (see Fig. 2), which is more representative.

As can be seen in Fig. 2, there are four possible sites that can be adsorption sites for H_2O molecules: these are S sites on the PS_4 tetrahedron (site ① in Fig. 2), S sites on the GeS_4 tetrahedron (site ② in Fig. 2), and Li sites between the PS_4 and GeS_4
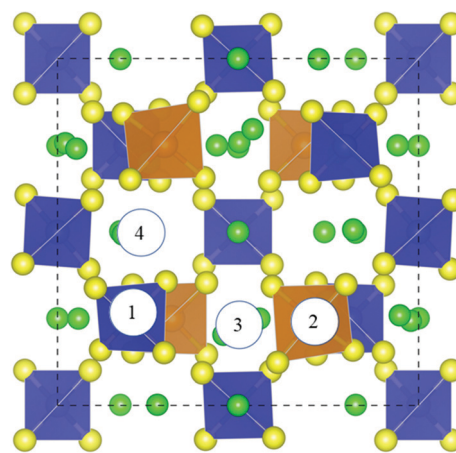

Fig. 2 H_2O adsorption site on the $Li_{10}GeP_2S_{12}$(110) surface. Site ① is the adsorption site on the PS_4 tetrahedron, site ② is the adsorption site on the GeS_4 tetrahedron, and sites ③ and ④ are the adsorption sites on Li$^+$.
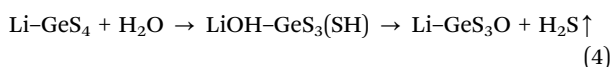
tetrahedra (sites ③ and ④ in Fig. 2). The adsorption energy (E_{ads}) is calculated as via eqn (2),

$$E_{ads} = E_{tot} - E_{H_2O} - E_{surface} \qquad (2)$$

where the E_{tot} is the total energy of the H_2O-adsorbed surface, E_{H_2O} is the energy of the H_2O molecule, and $E_{surface}$ is the total energy of the $Li_{10}GeP_2S_{12}$ slab. As listed in Table 2, we find that, compared with the S atoms in PS_4 tetrahedra and the S atoms in GeS_4 tetrahedra, H_2O molecules are more likely to be adsorbed on Li^+. For site ③, the adsorption energy of H_2O is -0.43 eV. This is because O sp³ hybridization in H_2O has an unshared electron pair, which can be combined with the vacant 2s orbital of the outermost layer of Li^+, thus forming the Li–O bond with greater adsorption energy.

We now investigate the decomposition of H_2O on the $Li_{10}GeP_2S_{12}(110)$ surface. According to the theoretical calculations of Mo et al.,[39] the reaction between the $Li_{10}GeP_2S_{12}(110)$ surface and H_2O is as follows:

$$Li-PS_4 + H_2O \rightarrow LiOH-PS_3(SH) \rightarrow Li-PS_3O + H_2S\uparrow \qquad (3)$$

$$Li-GeS_4 + H_2O \rightarrow LiOH-GeS_3(SH) \rightarrow Li-GeS_3O + H_2S\uparrow \qquad (4)$$

We show the reaction processes in Fig. 3. The adsorbed H_2O molecules can be decomposed into H^+ and OH^- on the surface, where H^+ reacts with the S atom on the PS_4/GeS_4 tetrahedra to form the H–S bond, and OH^- can be further decomposed to form O^{2-} and H^+. The latter H^+ reacts with S–H to form H_2S, which is desorbed from the (110) surface.

Fig. 4(a and b) depict the energy profile of the hydrolysis reaction between H_2O molecules and S of the PS_4 tetrahedra and the relative intermediate reaction products. IS0 stands for the (110) surface with no H_2O molecules adsorbed. IS1 stands for the (110) surface-adsorbed H_2O molecules. TS1 stands for the transition state and MS1 stand for the intermediate state of H_2O decomposed into H^+ and OH^-. MS2 stands for the second intermediate state, which relaxes the position of the H atom of OH^-, and MS3 stands for the third intermediate state of OH^- decomposition into H^+ and O^{2-}. FS stands for the final state of H_2S desorbing from the $Li_{10}GeP_2S_{12}(110)$ surface. From the results of Table 2, H_2O adsorbs on Li^+ and the adsorption energy is -0.43 eV. For the process from IS1 to MS1, H_2O decomposes into H^+ and OH^-, where H^+ combines with S to form the H–S bond and the related energy barrier is 0.41 eV. OH^- decomposes into H^+ and O^{2-} from MS2 to MS3, where H^+ combines with the SH group in MS1 to generate H_2S, which is adsorbed on the surface. Meanwhile, O^{2-} combines with S of GeS_4 to form the S–O bond, and the energy barrier for this is 0.65 eV. The process from MS3 to FS is the desorption of H_2S

from the surface, where the desorption energy is 0.27 eV. In addition, we also consider the similar reaction between H_2O and the GeS_4 tetrahedra on the $Li_{10}GeP_2S_{12}(110)$ surface, shown in Fig. 4(c and d). By comparing the energy profiles with different sulfur sources, we find that the reaction energy barrier of H_2O decomposition on the GeS_4 tetrahedra (0.80 eV, 0.72 eV) is higher than the reaction energy barrier on PS_4 tetrahedra (0.41 eV, 0.65 eV). This suggests that H_2O is more likely to react with S in the PS_4 tetrahedra in $Li_{10}GeP_2S_{12}$ to produce H_2S. FS in Fig. 4(b and d) also shows the result of an adsorbed oxygen atom and a sulfur vacancy. Since the reaction on the PS_4 tetrahedron is much easier than that on the GeS_4 tetrahedron, we now study the existence of S vacancies on the PS_4 tetrahedra.

As experiments have shown that the degradation of $Li_{10}GeP_2S_{12}$ releases a large amount of H_2S,[26] this process inevitably involves the sulfur atoms in the bulk. This means that S in $Li_{10}GeP_2S_{12}$ will migrate to the surface. As shown in Fig. 5, three diffusion paths of the S atom are considered: S atom diffusion on the surface, S atom diffusion from a GeS_4 tetrahedron to a PS_4 tetrahedron, and S atom diffusion from a PS_4 tetrahedron to a PS_4 tetrahedron, and Fig. 5(a) shows the energy barriers of 0.45 eV, 1.07 eV and 0.82 eV, respectively. Fig. 5(b) shows the initial and final structures for the diffusion of an S atom on the (110) surface. We find the presence of the Li^+ vacancy could be conducive to the diffusion of the S atom. This is because when the S atom diffuses from one tetrahedron to another tetrahedron, it could use the Li^+ channel along the c direction. Fig. 5(c and d) show the S atom diffusion path from a PS_4 tetrahedron to a PS_4 tetrahedron and from a GeS_4 tetrahedron to a PS_4 tetrahedron, respectively. The diffusion barriers shows that the diffusion of the S atom from a PS_4 tetrahedron to a PS_4 tetrahedron is relatively facile. This is also consistent with HSAB theory, where the bond of the soft base S and soft acid Ge is stronger than the bond of the soft base S and the hard acid P, and the bond energy of Ge–S is higher than that of P–S.

The decomposition of H_2O also leaves an oxygen atom on the surface, while experimental results of the continuous release of H_2S also show that those oxygen atoms do not form a protective layer on the surface to prevent $Li_{10}GeP_2S_{12}$ from contacting the air. This also means O atoms on the surface can diffuse into the bulk. Since Fig. 5 shows that a S atom can diffuse from a GeS_4 tetrahedron to a PS_4 tetrahedron in the bulk, S vacancies will concentrate on the GeS_4 tetrahedra. Therefore, oxygen atoms can diffuse from the surface to the bulk through the GeS_4 tetrahedra. Fig. 6(a) shows the energy barriers during the process of O diffusing from the surface to the bulk, an O atom diffusing from GeS_3O to PS_3O, and an O atom diffusing from PS_3O to PS_3O, for which the energy barriers are 0.21 eV, 1.99 eV and 2.72 eV, respectively. Fig. 6(b) shows the diffusion path of an oxygen atom from the surface to the bulk. The path through the GeS_4 tetrahedron into the bulk is found to have the lowest energy barrier (0.21 eV). However, the energy barriers for O atom diffusion in the bulk are 1.99 eV and 2.72 eV, which are too high for O atoms in the pristine $Li_{10}GeP_2S_{12}$ crystal. Thus, it is hard for O ions to diffuse in

Table 2 Adsorption energies of H_2O at different sites on the (110) surface

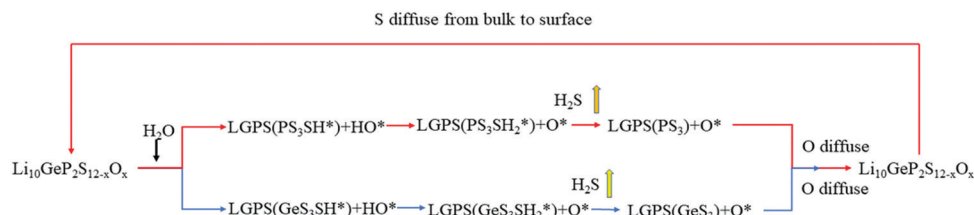| Site	①	②	③	④
E_{ads} (eV)	0.15	-0.12	-0.43	-0.28

Fig. 3 Reaction paths of $Li_{10}GeP_2S_{12}$ surfaces and H_2O, where the red path represents H_2O reacting with S in the PS_4 tetrahedra, and the blue one represents H_2O reacting with S in the GeS_4 tetrahedra.
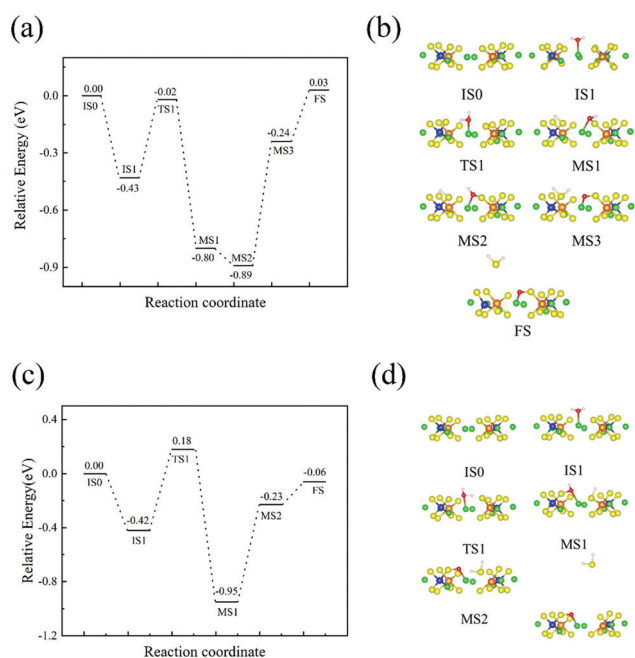

Fig. 4 Reaction path profiles of H_2O reactions on the $Li_{10}GeP_2S_{12}$(110) surface. (a) H_2O reaction energies related to the PS_4 tetrahedra; (b) structural diagram of the minimum energy path for the H_2O reaction with PS_4 tetrahedra; (c) H_2O reaction energy related to the GeS_4 tetrahedra; and (d) structural diagram of the minimum energy path for the double H_2O reaction with the GeS_4 tetrahedra. (IS, initial state; TS, transition state; MS, meta-stable state; FS, final state). Color code: green, Li atoms; yellow, S atoms; blue, P atoms; orange, Ge atoms; red, O atoms; white, H atoms.
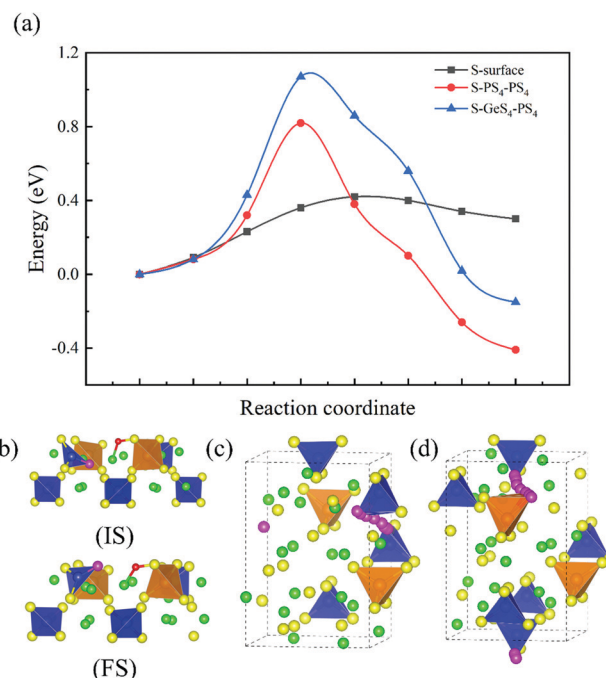

Fig. 5 Minimum energy paths for sulfur diffusion. (a) Energy profiles of S atom diffusion. (b) Structural diagram of S atom diffusion on the surface (IS, initial state; FS, final state). (c) Structural diagram of S atom diffusion in the bulk from a PS_4 tetrahedron to a PS_4 tetrahedron. (d) Diagram of S atom diffusion in the bulk from a GeS_4 tetrahedron to a PS_4 tetrahedron. Color code: green, Li atoms; yellow, S atoms; blue, P atoms; orange, Ge atoms; pink, the diffusing S atom.

the bulk. However, it will lead O ions being deposited in the same area, which will destroy the structure of $Li_{10}GeP_2S_{12}$, and this is also the cause of the miscellaneous peaks in the XRD pattern of $Li_{10}GeP_2S_{12}$ after exposure to air.[25]

According to the XRD patterns obtained by Sun *et al.*,[26] PO_4^{3-} is found in the product of $Li_{10}GeP_2S_{12}$ decomposition in the atmosphere. Mo *et al.*[29] also claimed that $Li_{10}GeP_2S_{12}$ is thermodynamically unstable. Considering the thermodynamic stability, we also calculated the thermodynamic stability of $Li_{10}GeP_2S_{12}$ after being exposed to the air and the degree to which it reacts with H_2O. Mo *et al.*[29] also found that $Li_{10}GeP_2S_{12}$ can be decomposed into Li_3PS_4 and Li_4GeS_4. The phase decomposition energy (ΔE_{pd}) of $Li_{10}GeP_2S_{12-x}O_x$ is calculated with

respect to the most stable ternary compounds (Li_3PS_4, Li_3PO_4, Li_4GeS_4, and Li_4GeO_4) to further check the phase stability. The ΔE_{pd} is defined as follows:

$$\Delta E_{pd}(x=0) = E(Li_3PS_4) + \frac{E(Li_4GeS_4)}{2} - E(Li_{10}GeP_2S_{12}) \quad (5)$$

$$\Delta E_{pd}(0 < x < 8) = \frac{[(8-x)E(Li_3PS_4) + xE(Li_3PO_4)]}{8} + \frac{E(Li_4GeS_4)}{2} - E(Li_{10}GeP_2S_{12-x}O_X) \quad (6)$$
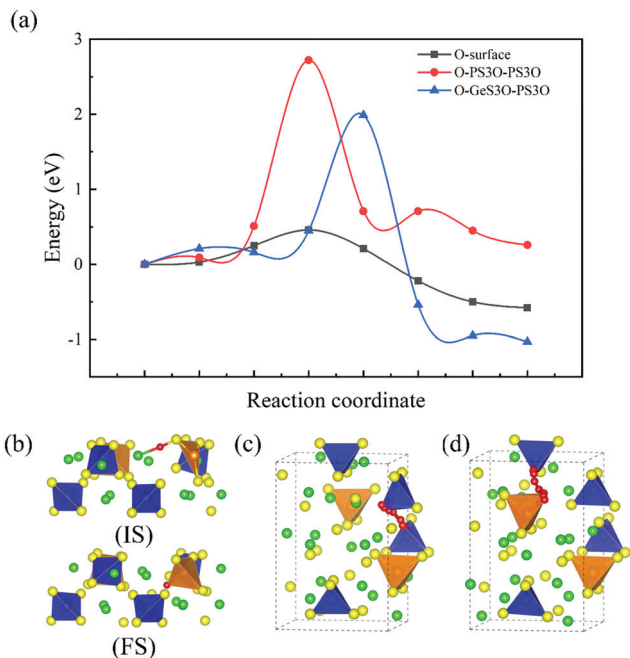
Fig. 6 Minimum energy paths for O atom diffusion. (a) Energy profiles for O atom diffusion. (b) Structural diagram of O atom diffusion from the surface into the bulk. (c) Structural diagram of O atom diffusion in the bulk from a PS_3O tetrahedron to a PS_3O tetrahedron. (d) Diagram of O atom diffusion in the bulk from a GeS_3O tetrahedron to a PS_3O tetrahedron. Color code: green, Li atoms; yellow, S atoms; blue, P atoms; orange, Ge atoms; red, O atoms.

$$\Delta E_{pd}(8 < x < 12) = \frac{[(12-x)E(Li_4GeS_4) + (x-8)E(Li_4GeO_4)]}{8} + 2E(Li_3PO_4) - E(Li_{10}GeP_2S_{12-x}O_X) \tag{7}$$

$$\Delta E_{pd}(x = 12) = 2E(Li_3PO_4) + E(Li_4GeO_4) - E(Li_{10}GeP_2S_{12-x}O_x) \tag{8}$$

A negative value of ΔE_{pd} indicates thermodynamic phase stability against decomposition. For the degree of reaction with H_2O in air, according to the reaction equilibrium $Li_{10}GeP_2S_{12}$ + $H_2O \rightarrow Li_{10}$ GeP_2O_{12} + H_2S, we define the energy of the generation of H_2S as ΔE_{H_2S}:

$$\Delta E_{H_2S} = E(Li_{10}GeP_2O_{12})/12 + E(H_2S) - E(Li_{10}GeP_2S_{12})/12 - E(H_2O) \tag{9}$$

A positive value of ΔE_{H_2S} indicates thermodynamic stability against H_2S generation. As shown in Fig. 7, we find that the value of ΔE_{pd} decreases as O atoms successively replace the S atoms in $Li_{10}GeP_2S_{12}$. This indicates that the thermal stability of $Li_{10}GeP_2S_{12}$ is continuously improved with the reaction. When x reaches 8 ($\Delta E_{H_2S} = 1.05$ eV), $Li_{10}GeP_2S_4O_8$ is inert to H_2O molecules in the air. At the same time, $Li_{10}GeP_2S_4O_8$ could be decomposed to Li_3PO_4 and Li_4GeS_4. This indicates that the S
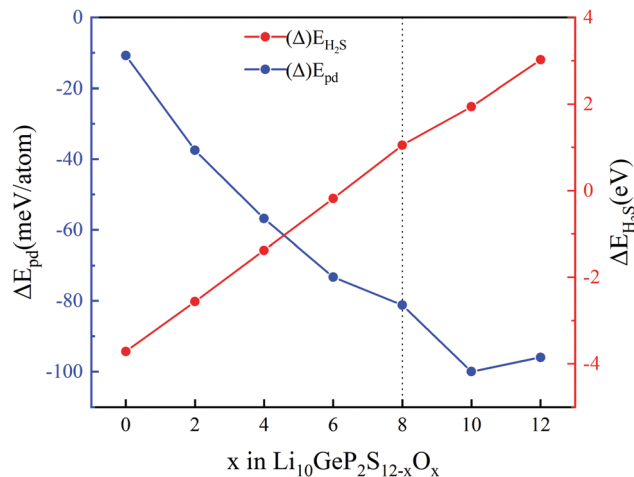

Fig. 7 Phase decomposition (pd) stability (ΔE_{pd}, reaction equilibrium in eqn (5)–(8)) and moisture stability with x in the $Li_{10}GeP_2S_{12-x}O_x$.

atoms of a PS_4 tetrahedron are completely replaced by O atoms, proving that S in H_2S comes from the PS_4 tetrahedra.

By doping with Sb, Sun *et al.* successfully inhibited $Li_{10}GeP_2S_{12}$ hydrolysis.[26] To analyze the mechanism, we investigated how Sb doping inhibits the hydrolysis of $Li_{10}GeP_2S_{12}$. For the possible doping locations of Sb *via* thermodynamic calculations, the Sb_P formation energy (E) was calculated using eqn (10):

$$E = E_{(xSb-LGPS)} + x \cdot E_P - E_{(LGPS)} - x \cdot E_{Sb} \tag{10}$$

We considered two Sb doping sites (on P_{2b} or P_{4d} sites) and five types of substitution (no Sb substitution, 100% on P_{2b} substitution, 100% on P_{4d} substitution, 50%P_{2b} + 50%P_{4d} substitution, and full substitution). The results of the formation energy when Sb occupies different P sites are shown in Table 3. We find that Sb is more inclined to occupy the P_{4d} sites. Fig. 8(a) shows the structure of $Li_{10}Ge(P_{1-x}Sb_x)_2S_{12}$ with Sb occupying P_{4d} sites. According to the previous calculation of surface energies, the (110) surface is more easily exposed. Fig. 8(b) shows the new surface when Sb is substituted on a surface P_{4d} site. Fig. 8(c) shows the energy profile of H_2O adsorption and reaction with an SbS_4 tetrahedron on the $Li_{10}Ge(P_{1-x}Sb_x)_2S_{12}(110)$ surface. Fig. 8(d) depicts the structures of the intermediates and the corresponding transition states during the reaction of H_2O and a SbS_4 tetrahedron on the $Li_{10}Ge(P_{1-x}Sb_x)_2S_{12}(110)$ surface. In the process from IS0 to IS1, H_2O molecules are adsorbed at the Li site, and the adsorption energy is −0.33 eV. For the process from IS1 to MS1, the H_2O molecule is decomposed to form H^+ and OH^-, while H^+ is bonded to the S on an SbS_4 tetrahedron forming SH. The decomposition barrier is 0.22 eV; meanwhile, it releases

Table 3 Relative energy with Sb doping at different P sites

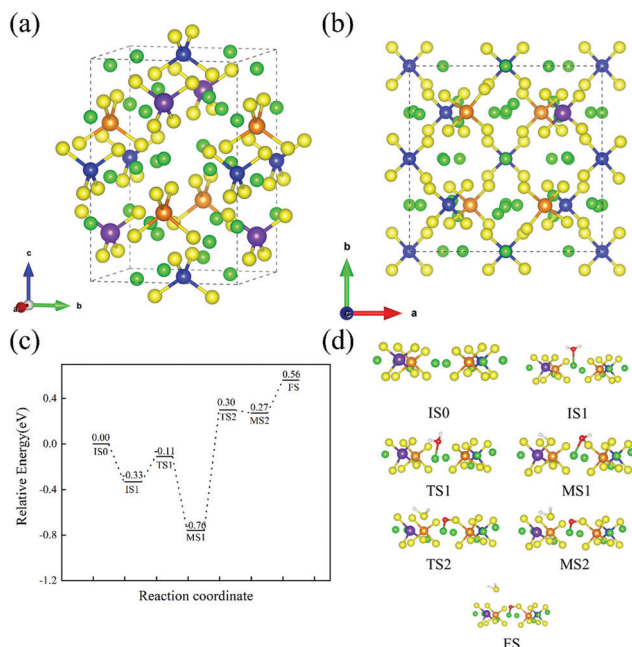| Sb	No doping	100% P_{2b}	100% P_{4d}	50% P_{2b} + 50% P_{4d}	Full doping
E (eV)	0	5.16	4.64	4.65	9.96

Fig. 8 (a) Crystal structure of Sb substitution on P_{4d} sites; (b) crystal structure of Sb substitution on a P_{4d} site on the (110) surface; (c) H_2O reaction energy profile on an SbS_4 tetrahedron of the $Li_{10}Ge(P_{1-x}Sb_x)_2S_{12}$(110) surface; and (d) structural diagram of the minimum energy path for the reaction of H_2O with an SbS_4 tetrahedron on the $Li_{10}Ge(P_{1-x}Sb_x)_2S_{12}$(110) surface. Color code: green, Li atoms; yellow, S atoms; blue, P atoms; orange, Ge atoms; red, O atoms; white, H atoms; purple, Sb atoms.
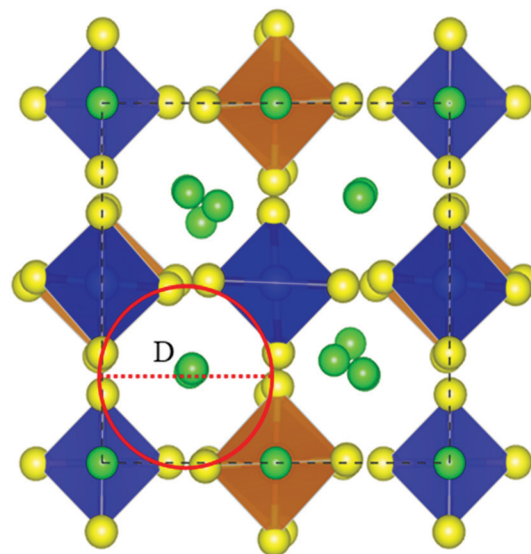

Fig. 9 Lithium-ion diffusion channel in the c-direction (red circle), where the channel radius is D. Color code: green, Li atoms; yellow, S atoms; blue, P atoms; orange, Ge atoms.

0.65 eV for this step. For the process from MS1 to MS2, OH^- is decomposed to form H_2S with HS adsorbed on the surface, while the remaining O atoms are adsorbed on Li atoms. The barrier of this step is 1.06 eV. MS2 to FS is the H_2S desorption process, which needs 0.29 eV. From the decomposition of H_2O molecules on SbS_4 tetrahedra, the maximum reaction barrier required for the reaction of an H_2O molecule with S in a SbS_4 tetrahedron to produce H_2S gas is 1.06 eV. In the previous calculation, the maximum energy barrier required for H_2O molecules to react with S in PS_4 tetrahedra to form H_2S gas was 0.65 eV. With the increased barrier of OH^- decomposition, the substitution of Sb can prevent the hydrolysis of $Li_{10}GeP_2S_{12}$.

In addition, we studied the effect of Sb doping on $Li_{10}GeP_2S_{12}$. The data in Table 4 show that with an increase in Sb doping, the lattice constants of $Li_{10}GeP_2S_{12}$ will also increase. Furthermore, the diffusion barrier of Li ions along the c direction will also increase, which is consistent with the

experimental findings of Sun et al.[26] that the conductivity of the Li ion decreases with Sb doping. The diffusion channel diameter (D) is defined as the average value of the minimum distances between tetrahedra along the c direction, as shown Fig. 9. From Table 4, we find that diffusion barrier (E_b) increases as D decreases.

Conclusion

Based on first principles calculations, we have unveiled the kinetic and thermodynamic mechanism in the reaction of $Li_{10}GeP_2S_{12}$ with H_2O molecules in air to produce H_2S gas. The surfaces of $Li_{10}GeP_2S_{12}$ exposed to the air are (001), (110) and (111), and H_2O molecules are adsorbed on Li^+ sites. The rate-determining step for the H_2S-releasing reaction is the decomposition of OH^- with an energy barrier of 0.65 eV. The S atoms can diffuse between PS_4 tetrahedra, and the diffusion barrier is 0.82 eV. Moreover, S can diffuse from the bulk to the surface with a diffusion energy barrier of 0.45 eV. The O atoms can diffuse from the surface into the bulk, and the diffusion energy barrier is 0.21 eV. According to the thermodynamic analysis, the formation of $Li_{10}GeP_2S_4O_8$ will inhibit the reaction with H_2O molecules and prevent the release of H_2S gas. Sb doping could also prevent the hydrolysis of $Li_{10}GeP_2S_{12}$ due to the increased energy barrier (1.06 eV) for the decomposition of H_2O on the SbS_4 tetrahedra. The diffusion barrier of the Li ions in $Li_{10}Ge(P_{1-x}Sb_x)_2S_{12}$ will also increase with the amount of Sb doping.

Conflicts of interest

There are no conflicts to declare.

Table 4 Lattice constants (a, and c), Li ion channel width D and Li ion diffusion barrier E_b in $Li_{10}Ge(P_{1-x}Sb_x)_2S_{12}$ related to the amount of Sb doping x

x	0	0.125	0.250	0.375	0.50
a (Å)	8.75	8.78	8.79	8.81	8.82
c (Å)	12.88	12.93	12.99	13.04	13.09
D (Å)	4.47	4.45	4.43	4.42	4.42
E_b (eV)	0.25	0.27	0.30	0.31	0.32

Acknowledgements

References

1 C. Zhang, C. Lu, F. Zhang, F. Qiu, X. Zhuang and X. Feng, Two-dimensional organic cathode materials for alkali-metal-ion batteries, *J. Energy Chem.*, 2018, **27**(1), 86–98.

2 X. Zhan, Z. Chen and Q. Zhang, Recent progress in two-dimensional COFs for energy-related applications, *J. Mater. Chem. A*, 2017, **5**(28), 14463–14479.

3 J. Xie, C. E. Zhao, Z. Q. Lin, P. Y. Gu and Q. Zhang, Nanostructured Conjugated Polymers for Energy-Related Applications beyond Solar Cells, *Chem. – Asian J.*, 2016, **11**(10), 1489–1511.

4 W. Liu, X. Li, D. Xiong, Y. Hao, J. Li, H. Kou, B. Yan, D. Li, S. Lu, A. Koo, K. Adair and X. Sun, Significantly improving cycling performance of cathodes in lithium ion batteries: The effect of Al_2O_3 and $LiAlO_2$ coatings on $LiNi_{0.6}Co_{0.2}Mn_{0.2}O_2$, *Nano Energy*, 2018, **44**, 111–120.

5 Y. Chu, Y. Shen, F. Guo, X. Zhao, Q. Dong, Q. Zhang, W. Li, H. Chen, Z. Luo and L. Chen, Advanced Characterizations of Solid Electrolyte Interphases in Lithium-Ion Batteries, *Electrochem. Energy Rev.*, 2020, **3**, 187–219.

6 P.-J. Lian, B.-S. Zhao, L.-Q. Zhang, N. Xu, M.-T. Wu and X.-P. Gao, Inorganic sulfide solid electrolytes for all-solid-state lithium secondary batteries, *J. Mater. Chem. A*, 2019, **7**(36), 20540–20557.

7 D. Monroe, Building a better battery, *MRS Bull.*, 2020, **45**(3), 246–247.

8 F. Zheng, M. Kotobuki, S. Song, M. O. Lai and L. Lu, Review on solid electrolytes for all-solid-state lithium-ion batteries, *J. Power Sources*, 2018, **389**, 198–213.

9 G. Zhou, F. Li and H.-M. Cheng, Progress in flexible lithium batteries and future prospects, *Energy Environ. Sci.*, 2014, **7**(4), 1307–1338.

10 E. Quartarone and P. Mustarelli, Electrolytes for solid-state lithium rechargeable batteries: recent advances and perspectives, *Chem. Soc. Rev.*, 2011, **40**(5), 2525–2540.

11 X. Han, Y. Gong, K. K. Fu, X. He, G. T. Hitz, J. Dai, A. Pearse, B. Liu, H. Wang, G. Rubloff, Y. Mo, V. Thangadurai, E. D. Wachsman and L. Hu, Negating interfacial impedance in garnet-based solid-state Li metal batteries, *Nat. Mater.*, 2017, **16**(5), 572–579.

12 Y. Ren, K. Chen, R. Chen, T. Liu, Y. Zhang, C.-W. Nan and B. Vyas, Oxide Electrolytes for Lithium Batteries, *J. Am. Ceram. Soc.*, 2015, **98**(12), 3603–3623.

13 W. Xiao, J. Wang, L. Fan, J. Zhang and X. Lia, Recent advances in $Li_{1+x}Al_xTi_{2-x}(PO_4)_3$ solid-state electrolyte for safe lithium batteries, *Energy Storage Mater.*, 2019, **19**, 379.

14 E. Rangasamy, Z. Liu, M. Gobet, K. Pilar, G. Sahu, W. Zhou, H. Wu, S. Greenbaum and C. Liang, An iodide-based $Li_7P_2S_8I$ superionic conductor, *J. Am. Chem. Soc.*, 2015, **137**(4), 1384–1387.

15 Y. Kato, S. Hori, T. Saito, K. Suzuki, M. Hirayama, A. Mitsui, M. Yonemura, H. Iba and R. Kanno, High-power all-solid-state batteries using sulfide superionic conductors, *Nat. Energy*, 2016, **1**, 4.

16 F. Wu, W. Fitzhugh, L. Ye, J. Ning and X. Li, Advanced sulfide solid electrolyte by core-shell structural design, *Nat. Commun.*, 2018, **9**(1), 4037.

17 H. Muramatsu, A. Hayashi, T. Ohtomo, S. Hama and M. Tatsumisago, Structural change of $Li_2S–P_2S_5$ sulfide solid electrolytes in the atmosphere, *Solid State Ionics*, 2011, **182**(1), 116–119.

18 T. Kaib, S. Haddadpour, M. Kapitein, P. Bron, C. Schröder, H. Eckert, B. Roling and S. Dehnen, New Lithium Chalcogenidotetrelates, LiChT: Synthesis and Characterization of the Li^+-Conducting Tetralithium ortho-Sulfidostannate Li_4SnS_4, *Chem. Mater.*, 2012, **24**(11), 2211–2219.

19 K. Kanazawa, S. Yubuchi, C. Hotehama, M. Otoyama, S. Shimono, H. Ishibashi, Y. Kubota, A. Sakuda, A. Hayashi and M. Tatsumisago, Mechanochemical Synthesis and Characterization of Metastable Hexagonal Li_4SnS_4 Solid Electrolyte, *Inorg. Chem.*, 2018, **57**(16), 9925–9930.

20 K. H. Park, D. Y. Oh, Y. E. Choi, Y. J. Nam, L. Han, J. Y. Kim, H. Xin, F. Lin, S. M. Oh and Y. S. Jung, Solution-Processable Glass LiI-Li_4SnS_4 Superionic Conductors for All-Solid-State Li-Ion Batteries, *Adv. Mater.*, 2016, **28**(9), 1874–1883.

21 G. Sahu, Z. Lin, J. Li, Z. Liu, N. Dudney and C. Liang, Air-stable, high-conduction solid electrolytes of arsenic-substituted Li_4SnS_4, *Energy Environ. Sci.*, 2014, **7**(3), 1053–1058.

22 Z. Zhang, J. Zhang, Y. Sun, H. Jia, L. Peng, Y. Zhang and J. Xie, Li_4-Sb Sn_1-S_4 solid solutions for air-stable solid electrolytes, *J. Energy Chem.*, 2020, **41**, 171–176.

23 H. Kwak, K. H. Park, D. Han, K.-W. Nam, H. Kim and Y. S. Jung, Li^+ conduction in air-stable Sb-Substituted Li_4SnS_4 for all-solid-state Li-Ion batteries, *J. Power Sources*, 2020, **446**.

24 R. G. Pearson, Hard and soft acids and bases, HSAB, part 1: Fundamental principles, *J. Chem. Educ.*, 1968, **45**, 9.

25 A. Hayashi, H. Muramatsu, T. Ohtomo, S. Hama and M. Tatsumisago, Improvement of chemical stability of Li_3PS_4 glass electrolytes by adding M_xO_y (M = Fe, Zn, and Bi) nanoparticles, *J. Mater. Chem. A*, 2013, **1**, 21.

26 J. Liang, N. Chen, X. Li, X. Li, K. R. Adair, J. Li, C. Wang, C. Yu, M. Norouzi Banis, L. Zhang, S. Zhao, S. Lu, H. Huang, R. Li, Y. Huang and X. Sun, $Li_{10}Ge(P_{1-x}Sb_x)_2S_{12}$ Lithium-Ion Conductors with Enhanced Atmospheric Stability, *Chem. Mater.*, 2020, **32**(6), 2664–2672.

27 N. Kamaya, K. Homma, Y. Yamakawa, M. Hirayama, R. Kanno, M. Yonemura, T. Kamiyama, Y. Kato, S. Hama,

K. Kawamoto and A. Mitsui, A lithium superionic conductor, *Nat. Mater.*, 2011, **10**(9), 682–686.

28 S. Adams and R. Prasada Rao, Structural requirements for fast lithium ion migration in $Li_{10}GeP_2S_{12}$, *J. Mater. Chem.*, 2012, **22**(16), 7687–7691.

29 Y. Mo, S. P. Ong and G. Ceder, First Principles Study of the $Li_{10}GeP_2S_{12}$ Lithium Super Ionic Conductor Material, *Chem. Mater.*, 2011, **24**(1), 15–17.

30 X. Liang, L. Wang, Y. Jiang, J. Wang, H. Luo, C. Liu and J. Feng, In-Channel and In-Plane Li Ion Diffusions in the Superionic Conductor $Li_{10}GeP_2S_{12}$ Probed by Solid-State NMR, *Chem. Mater.*, 2015, **27**(16), 5503–5510.

31 A. Miura, N. C. Rosero-Navarro, A. Sakuda, K. Tadanaga, N. H. H. Phuc, A. Matsuda, N. Machida, A. Hayashi and M. Tatsumisago, Liquid-phase syntheses of sulfide electrolytes for all-solid-state lithium battery, *Nat. Rev. Chem.*, 2019, **3**(3), 189–198.

32 Y. Wang, Z. Liu, X. Zhu, Y. Tang and F. Huang, Highly lithium-ion conductive thio-LISICON thin film processed by low-temperature solution method, *J. Power Sources*, 2013, **224**, 225–229.

33 J. P. Perdew, K. Burke and M. Ernzerhof, Generalized gradient approximation made simple (vol 77, pg 3865, 1996), *Phys. Rev. Lett.*, 1997, **78**(7), 1396.

34 P. E. Blochl, Projector augmented-wave method, *Phys. Rev. B: Condens. Matter Mater. Phys.*, 1994, **50**(24), 17953–17979.

35 G. Kresse and D. Joubert, From ultrasoft pseudopotentials to the projector augmented-wave method, *Phys. Rev. B: Condens. Matter Mater. Phys.*, 1999, **59**(3), 1758–1775.

36 G. Kresse and J. Furthmuller, Efficient iterative schemes for ab initio total-energy calculations using a plane-wave basis set, *Phys. Rev. B: Condens. Matter Mater. Phys.*, 1996, **54**(16), 11169–11186.

37 G. Henkelman, B. P. Uberuaga and H. Jónsson, A climbing image nudged elastic band method for finding saddle points and minimum energy paths, *J. Chem. Phys.*, 2000, **113**(22), 9901–9904.

38 K. Oh, D. Chang, B. Lee, D.-H. Kim, G. Yoon, I. Park, B. Kim and K. Kang, Native Defects in $Li_{10}GeP_2S_{12}$ and Their Effect on Lithium Diffusion, *Chem. Mater.*, 2018, **30**(15), 4995–5004.

39 Y. Zhu and Y. Mo, Materials Design Principles for Air-Stable Lithium/Sodium Solid Electrolytes, *Angew. Chem., Int. Ed.*, 2020, **59**(40), 17472–17476.